AIP | Journal of Applied Physics

Magnetization reversal in magnetic dot arrays: Nearest-neighbor interactions and global configurational anisotropy

Ben Van de Wiele, Samuele Fin, Matteo Pancaldi, Paolo Vavassori, Anandakumar Sarella, and Diego Bisero

Citation: Journal of Applied Physics **119**, 203901 (2016); doi: 10.1063/1.4949554
View online: http://dx.doi.org/10.1063/1.4949554
View Table of Contents: http://scitation.aip.org/content/aip/journal/jap/119/20?ver=pdfcov
Published by the AIP Publishing

Magnetization reversal in magnetic dot arrays: Nearest-neighbor interactions and global configurational anisotropy

Ben Van de Wiele,[1] Samuele Fin,[2] Matteo Pancaldi,[3] Paolo Vavassori,[3,4] Anandakumar Sarella,[5] and Diego Bisero[2,6]
[1]*Department of Electrical Energy, Systems and Automation, Ghent University, Technologiepark 913, B-9052 Ghent-Zwijnaarde, Belgium*
[2]*Dipartimento di Fisica e Scienze della Terra, Università degli Studi di Ferrara, 44122 Ferrara, Italy*
[3]*CIC nanoGUNE, E-20018 Donostia-San Sebastian, Spain*
[4]*IKERBASQUE, Basque Foundation for Science, E-48013 Bilbao, Spain*
[5]*Physics Department, Mount Holyoke College, 211 Kendade, 50 College St., South Hadley, Massachusetts 01075, USA*
[6]*CNISM, Unità di Ferrara, 44122 Ferrara, Italy*

(Received 3 March 2016; accepted 29 April 2016; published online 24 May 2016)

Various proposals for future magnetic memories, data processing devices, and sensors rely on a precise control of the magnetization ground state and magnetization reversal process in periodically patterned media. In finite dot arrays, such control is hampered by the magnetostatic interactions between the nanomagnets, leading to the non-uniform magnetization state distributions throughout the sample while reversing. In this paper, we evidence how during reversal typical geometric arrangements of dots in an identical magnetization state appear that originate in the dominance of either Global Configurational Anisotropy or Nearest-Neighbor Magnetostatic interactions, which depends on the fields at which the magnetization reversal sets in. Based on our findings, we propose design rules to obtain the uniform magnetization state distributions throughout the array, and also suggest future research directions to achieve non-uniform state distributions of interest, e.g., when aiming at guiding spin wave edge-modes through dot arrays. Our insights are based on the Magneto-Optical Kerr Effect and Magnetic Force Microscopy measurements as well as the extensive micromagnetic simulations. *Published by AIP Publishing.*
[http://dx.doi.org/10.1063/1.4949554]

INTRODUCTION

The arrays of magnetic nanodots attract considerable interest to implement magnetic ultrahigh-density memories, information processing, and magnetic sensing. In these applications, the dimensions and the interdistances between the magnetic dots progressively reduce aiming at the increasing memory densities and the integration in devices with ever smaller dimensions.[1–3] Such miniaturization not only impedes a precise control of the individual magnetization states within the arrays[4] as required for memory applications but also amplifies collective spin wave properties that can be exploited in the design of high-frequency nano-oscillators and magnonic crystals.[5–10] By tuning the material and the geometry parameters (array periodicity, dot dimensions, and dot interdistances), one can optimize the spin wave properties—e.g., presence of dispersion band gaps—towards specific applications. However, these advantageous collective properties are only fully present when all dots in the array are in an identical magnetization state.[11] In contrast to these spin wave bulk-modes, spin wave edge-modes[12,13] are known to propagate along the edges of dot arrays as well as along internal boundaries, e.g., defined by regions with different ground states. Hence, controlling the non-uniformity in magnetization states might open new opportunities to dynamically (re)define the propagation paths for spin-wave edge modes, using globally applied magnetic fields. This would allow a reconfigurable routing of spin wave signals.

Recent publications[14,15] show that the magnetization reversal in dot arrays depends not only on the nanomagnet dimensions and arrangement but also on the global shape and dimension of the array itself. The finite size of the array introduces a global non-uniformity in magnetization states and location-dependent state transitions throughout the array. This "Global Configurational Anisotropy (GCA)" manifests itself due to the long-range magnetostatic interaction and strongly influences the magnetization states encountered during the array reversal process. In this publication, we additionally investigate the effect of "Nearest-Neighbor Magnetostatic (NNM)" interactions in the dot array. These are directly correlated with the magnetic charge distribution characteristic to the dot magnetization state and with the array lattice symmetry and spacing. We provide an in-depth insight in the competition between GCA and NNM interactions based on the extensive micromagnetic simulations, experimentally supported by Magneto-Optical Kerr Effect (MOKE) measurements and Magnetic Force Microscopy (MFM) imaging on arrays with identical global dimension and fixed periodicity, but different dot dimensions. This allows us to understand the origin of typical arrangements of magnetization states throughout the dot array and relate them to the dominating long- or short-range magnetostatic interactions.

FABRICATION, MEASUREMENTS, AND SIMULATIONS

Magnetic dot arrays are fabricated on a Si(100) chip of $10 \times 10\,\mathrm{mm}^2$ by electron beam lithography processing. The

desired pattern is drawn with an electron beam on electron sensitive resist layers, previously coated on the Si(100) substrate. The electron sensitive resist has a double layer of poly(methyl methacrylate) (DL-PMMA) with the bottom and top layers consisting of PMMA 495 K A2 and PMMA 950 K A2, respectively. A RAITH 150TWO electron beam lithography tool is employed. The patterns on the DL-PMMA are generated using an acceleration voltage of 10 kV, 10 μm aperture, and a measured current of 20 pA. Subsequently, a permalloy layer is deposited at a rate of 0.6 Å/s onto the electron-beam lithography structured sample using an electron-beam evaporator. The thickness is varied between different samples. Finally, the DL-PMMA is removed in a lift-off process, leaving the desired arrays of permalloy dots on the silicon substrate. The created patterns are arrays of 16×16 circular nanodots arranged in a square network with a periodicity of 400 nm. In what follows, we mainly concentrate on arrays with 315 nm wide dots and thicknesses ranging from 10 nm to 45 nm. Figure 1(a) shows an SEM micrograph of an array with 315 nm wide and 23 nm thick dots.

Magneto-Optical Kerr Effect Magnetometry (MOKE) measurements are performed using an optical wide-field polarization microscope optimized for Kerr microscopy, while applying an arbitrary in-plane field.[16] Complementary Magnetic Force Microscopy (MFM) images are recorded by a Digital Instruments Nanoscope IIIa in the phase detection mode, i.e., monitoring the cantilever's phase of oscillation while the magnetic tip is scanning the sample surface at an average distance of 70 nm (lift mode).[17,18] Commercially available ferromagnetic CoCr tips are used. The MFM measurements are performed at successive in-plane fields ranging from +80 mT to −80 mT. Different scanning directions and tip-to-sample distances were used to verify that the obtained MFM images do not depend on the operating conditions.

Micromagnetic simulations are performed using MuMax3[19] which allows the simulation of the hysteresis loop for the entire array without applying periodic boundary conditions. The simulations are carried out starting from saturation and reducing the applied field with steps of 1 mT. After every field jump, the magnetization processes are computed for 50 ns. A high damping $\alpha = 1$ ensures that the system is in equilibrium after this time span (we verified in a few cases that assuming $\alpha = 1$ instead of 0.015 does not alter the reversal process in terms of sequence and structure of the field induced metastable states). The saturation magnetization $M_S = 740 \times 10^3$ A/m and the negligible anisotropy are experimentally verified. Furthermore, an exchange stiffness $A = 1.2 \times 10^{-11}$ J/m is considered. Cells of $6.25\,\text{nm} \times 6.25\,\text{nm} \times T$ are used to discretize the sample (1024×1024 cells, T is the sample thickness). While figures report only on arrays with

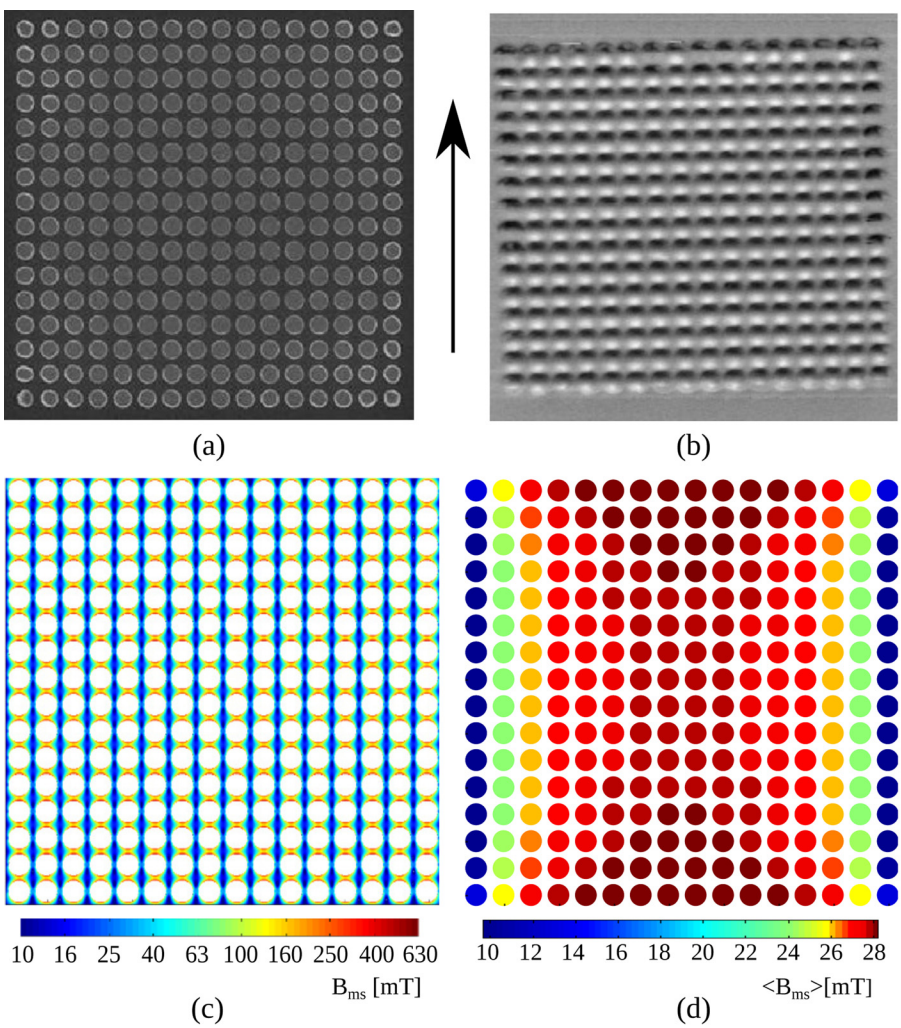

FIG. 1. (a) Experimental SEM image of the considered sample with dot diameters 315 nm and thickness 23 nm, (b) MFM image under a saturating external field applied along the direction of the central arrow, (c) local magnetostatic fields B_{ms} between the dots, and (d) averaged over each individual dot, the amplitude of the total magnetostatic field $\langle B_{ms} \rangle$ generated by all other nanomagnets in the array. Panels (b)–(d) are simulated under identical saturating field conditions.

315 nm wide dots, separation distance 85 nm, and varying thickness, we also performed simulations of dot arrays with fixed thickness and varying dot width to broaden our conclusions.

RESULTS AND DISCUSSION

In all our measurements and simulations, we first imposed single domain magnetization states throughout the complete array by applying a large in-plane magnetic field, parallel to a major symmetry axis of the array, namely, either horizontal or vertical. In the saturated state induced by a large vertical field, magnetic charges with an opposite sign concentrate at the top and bottom edges of each dot to generate a demagnetizing field opposing the magnetization in each individual dot. At the array space scale, the nanodots now act as the magnetic dipoles interacting with each other via the magnetostatic interaction. The dipoles align with the applied field and form vertical magnetization chains in which magnetic charges of neighboring dots compensate each other. In the MFM image of Fig. 1(b), this is reflected by the appearance of successive black and white spots along the columns of the array and in the simulated image of Fig. 1(c) by the high magnetostatic field intensities existing between vertically neighboring dots. The charge compensation is not achieved at the array boundaries due to the translation symmetry breaking at the sample edges, a fact that we will discuss later and is of fundamental importance. We refer to this local interaction as the *Nearest-Neighbor Magnetostatic (NNM)* interaction.

The nanomagnets also interact magnetostatically on the long-range: the dipolar field generated by each individual dipole (dot) in the array contributes to the total magnetostatic field. This field is non-uniform because of the finite dimensions of the array. Figure 1(d) shows, averaged in each dot, the amplitude of the total dipolar field that is generated by all other nanomagnets in the array (simulation). Compared to the bulk of the array, the dots located towards the left and right edges [top and bottom edges] of the array sense a progressively smaller [larger] magnetostatic field due to an increased asymmetric distribution of neighboring dots. Note that also the orientation of the total magnetostatic field varies throughout the array. However, for the saturated state of Fig. 1, variations in orientation are small. This geometry-dependent non-uniformity of the magnetostatic field present at the dot space scale is known as *Global Configurational Anisotropy (GCA)*.[14,15]

Let us now investigate how NNM interactions and GCA influence the magnetization reversal of the array. Figure 2 shows the measured (MOKE) and simulated hysteresis loops together with the distribution of simulated magnetization states during reversal (increasing branch). Interestingly, around remanence, there is a coexistence of S-states and vortex states (Fig. 2(b)). Once in the vortex state, the vortex cores gradually shift towards the dot edges for increasing fields, in a direction perpendicular to the applied field. This results in a gradual increase of the in-plane dot magnetization $\langle M_{xy}\rangle_{\mathrm{dot}}$, see Fig. 2(b). At a large threshold field, the vortex cores are expelled from the dots, again resulting in the uniform magnetization states, now pointing to the opposite

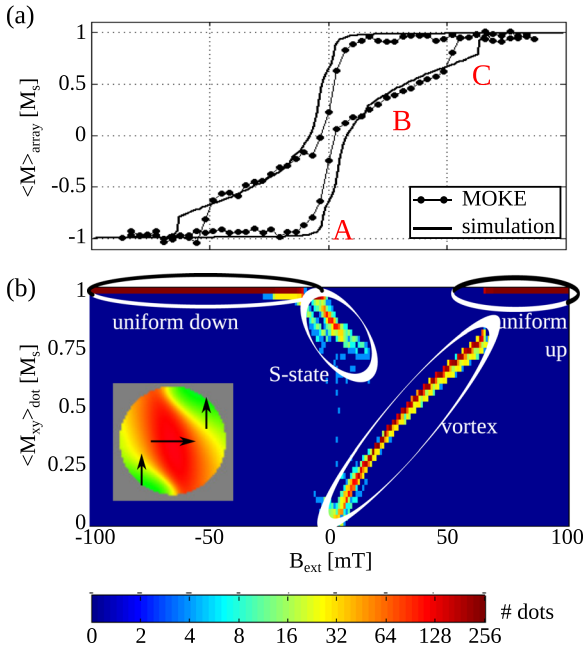

FIG. 2. (a) Hysteresis loops measured with MOKE (dots) and simulated (full line) of an 16 × 16 square array of 23 nm thick nanodots with diameter 315 nm and separation distance 85 nm. (b) Simulated distribution of the magnetization states when running through the increasing hysteresis branch. The states are characterized by their average in-plane magnetization $\langle M_{xy}\rangle_{dot} = \sqrt{\langle M_x\rangle_{dot}^2 + \langle M_y\rangle_{dot}^2}$. The colors represent the number of dots with a given $\langle M_{xy}\rangle_{dot}$. Note the coexistence of S-states and vortex states. Inset: magnetization distribution of an S-state.

direction. The correspondence in Fig. 2(a) between measured (MOKE) and simulated hysteresis loops confirms the state transitions: (i) the S- and vortex state coexistence gives rise to the non-zero remanence and, consequently, a loop with a coercive field as denoted by "A"; (ii) the gradual vortex core shifts lead to the long magnetization tails—denoted by "B"; and (iii) the vortex core expulsions result in a sudden magnetization jump to saturation—denoted by "C." Note that the experimental loop is slightly narrower compared to the simulated one as the transition processes in the real sample initiate earlier due to a non-zero temperature and the presence of structural disorder and fabrication imperfections which are absent in the simulation.

Figure 3 (top row) shows some magnetization snapshots in the field range where S-states and vortex states coexist together with the simulated and measured (MOKE) hysteresis loops of the simulated sample. At remanence ($B_{\mathrm{ext}} = 0$ mT), only dots near the sample corners reverted to the vortex state, leaving a large central domain with striking circular shape in the S-state. As a vortex state has negligible magnetic charges at the dot edges, it can be interpreted as a vanishing dipole which only weakly interacts with the nearest neighbors and has negligible contribution to the long-range magnetostatic field. Hence, the remanent state of Fig. 3(a) represents a circular array of interacting dipoles. In such configuration, GCA turns almost uniform, similar to the uniform demagnetizing fields found in dots with elliptical shape. When further reducing the field ($B_{\mathrm{ext}} = -4$ mT in Fig. 3(a)), vertical chains of vortex states start to creep into the bulk of the array. However, smaller ellipse-shaped domains of S-states can still

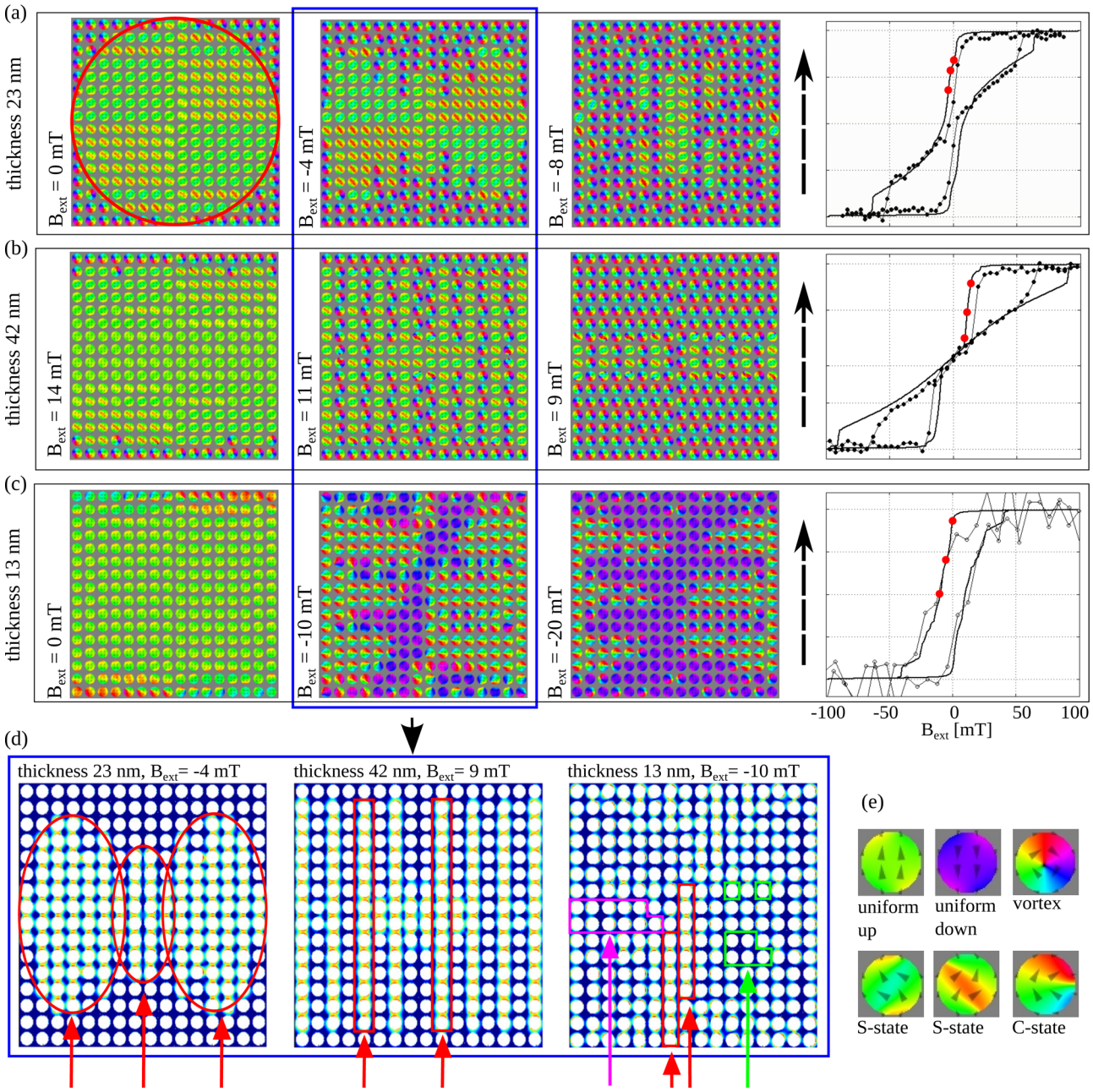

FIG. 3. (a)–(c) Magnetization distributions in the dot arrays with respective thicknesses of 23 nm, 42 nm, and 13 nm during reversal along with the hysteresis loops measured with MOKE (dots) and simulated with MuMax3 (full lines). The dots are 315 nm wide and have separation distance 85 nm. A large, saturating external field pointing in the direction indicated with the dashed arrows is slowly reduced. The magnetization distributions (simulated) correspond with the states indicated with red in the hysteresis loop. As a guide for the eye, the red circle in the left panel of (a) encloses the dots that are still in the S-state. (d) Simulated local magnetostatic fields B_{ms} between the dots for the central magnetization states of panels (a)–(c). The regions enclosed by red boundaries contain S-states: the elliptical shape in the left image results from the GCA dominance, the long magnetization chains parallel to the field direction result from the NNM dominance. In the right image, the regions enclosed by fuchsia boundaries contain C-states: The NNM interactions play in the direction perpendicular to the applied field; the regions enclosed by green boundaries contain isolated non-interacting clusters of vortex states. (e) Simulated magnetization states observed during the reversal process of the different arrays.

be identified, see also Fig. 3(d) (left) highlighted in red. At $B_{ext} = -8$ mT, additional vertical vortex chains break up the ellipse symmetries.

The presence of these vertical vortex chains originates in NNM interactions. Figure 1(c) already showed how dots in the uniform magnetization state magnetostatically interact with their neighbors positioned along the vertical direction. The dots in the top and bottom rows of the array have uncompensated magnetostatic charges and are thus less stable compared to the dots in the bulk. Consequently, when the field is reduced, these outer dots will be the first to revert to the vortex state resulting in uncompensated magnetostatic charges in the next dot in the chain and thus possibly initiating transitions there too. Micromagnetic simulations show that such highly dynamic avalanche processes are responsible for the formation of the vertical vortex chains observed in our samples. Such vortex chains are also observed in Ref. 20.

In thicker samples, the vortex state becomes more stable, leading to an earlier creation and later annihilation of vortices when running through the hysteresis loop, see, e.g., the 42 nm thick sample of Fig. 3(b). This is similar to isolated dots.[11] Additionally, our simulations indicate that the strength of the NNM interactions grows faster compared to GCA as the thickness of the dots increases. While the variations in $\langle B_{ms} \rangle$, Fig. 1(d), only increase moderately with sample thickness, the charge density near the dot edges that link neighboring dots in chains increases linearly with the sample thickness. In Fig. 3(b), this is clearly visible. Initially, the state transitions appear at the top and bottom rows of the array, very similar to the magnetization state observed in the 23 nm thick sample ($B_{ext} = 0$ mT) which was clearly GCA-dominated. However, when further reducing the field, the stronger NNM interactions initiate long transition avalanches that often cross the complete array ($B_{ext} = 11$ mT) and finally result in an array with only vortex states (slightly after $B_{ext} = 9$ mT). The dominance of NNM interaction and the consequent abundance of vortex states in thick samples is highly reflected in their hysteresis loops (Fig. 3, last column): while in the 23 nm thick sample, we observed a loop with non-zero remanence and coercive field, and we now find a zero-remanence and a zero coercivity in the 42 nm thick sample. The agreement between the measured and simulated hysteresis loops strongly supports the validity of the simulations and their analysis.

Figure 4 further examines the influence of sample thickness on vortex formation and annihilation. It shows the number of dots in the vortex state when going through the descending branch of the hysteresis loop, depending on the thickness of the simulated sample. In samples thicker than 30 nm, vortex nucleation fields linearly depend on the sample thickness, a behavior that is very similar to the isolated dots. Indeed, the distribution of nucleation fields is determined here by the conditions at which the dots at the array edge go to the vortex state and trigger transition avalanches due to the NNM interactions. A clearly different behavior is observed between 15 nm and 30 nm, where the vortex nucleation fields barely depend on the sample thickness. Here, the array reversal is dominated by GCA.

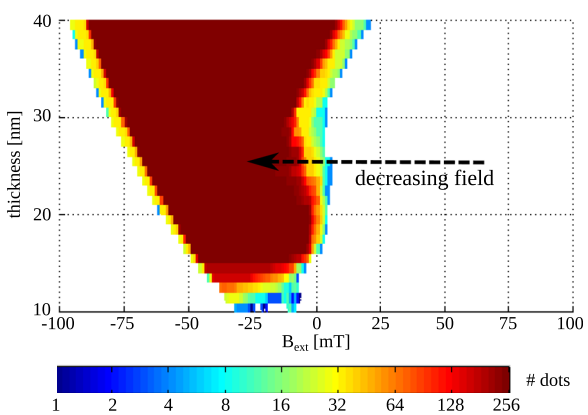

FIG. 4. Simulated number of dots in the vortex state for samples containing 16×16 dots with diameter 315 nm and separation distance 85 nm. The thickness is varied between the samples. A 100 mT external field is first applied and then gradually reduced to −100 mT as indicated by the dashed arrow.

In yet thinner samples, the stability of vortex states is severely reduced. Consequently, the hysteresis loops of the 13 nm thick sample (Fig. 3(c)) are more squared, i.e., have larger coercive fields, and have only very small magnetization tails. In Fig. 4, we can see that not all dots pass through the vortex state while reversing and that—if obtained—the vortex state is only stable in a small field window. Alternatively, the C-state is stabilized.[11,21] This magnetization state corresponds with a partially accomplished aspiration of the system to remove magnetic charges at the dot edges. Although the latter is achieved most efficiently in vortex states, the vortex creation comes at an increasingly high cost as thickness reduces (mostly due to magnetostatic energy in the vortex core). As a compromise, C-states are formed that properly remove the opposite magnetic charges from the applied field direction and displace them close to each other, at one side of the dot (e.g., to the right edge in Fig. 3(e)). The closely spaced opposite charges do not annihilate to form a vortex core as this is energetically unfavorable. The horizontal charge arrangement of the C-state contrasts the vertical one characteristic to the uniform and S-state and the negligible edge charges characteristic to the vortex state. Consequently, the NNM interactions now induce a tendency to form horizontally stretched domains with dots in the C-state, Fig. 3(c). Figure 3(d) (right) shows how (i) dots in the S-state form vertical magnetization chains—red; (ii) dots in the C-state form horizontally stretched domains—fuchsia; and (iii) clusters of dots in the vortex state form isolated non-interacting islands—green. Closer to the coercive field ($B_{ext} = -20$ mT), the characteristic horizontally arranged magnetization regions become even more apparent. Note that the magnetization state at $B_{ext} = 0$ mT is still GCA-dominated.

While the agreement between the simulated and measured hysteresis loops of Fig. 3 strongly suggests the correctness of the micromagnetic description, we now aim at getting a direct confirmation based on the MFM measurements. The MFM results reported in Fig. 5 have been verified changing the tip's scanning direction with respect to the applied field direction. The effects of GCA and NNM interactions confirmed to be stable and independent on the specific experimental conditions. Still the direct comparison of MFM with micromagnetic simulations and MOKE is highly impeded by the effect of the MFM tip on the magnetization. The stray field of the magnetic tip furnishes a small amount of energy that enables magnetization transitions to take place earlier in the reversal process and may even facilitate transitions that were not accessible without the tip's stray field. This effect is well known[22–25] and is also observed in our MFM measurements, see Fig. 5. In the images, a black-white contrast corresponds to the dots in the uniform or S-state, and a more uniform gray color characterizes the vortices. The C-states are not observed, even on higher resolution measurements. Since they are only metastable,[21] we expect them to have instantaneously switched to the vortex state under the action of the MFM tip. The MFM images of the 13 nm thick sample (Fig. 5(a)) evidence a clear manifestation of the GCA effect as found in the micromagnetic simulations with thicknesses between 15 nm and 30 nm. The images of the 28 nm thick sample (Fig. 5(b)) show that GCA initiates the reversal process around $B_{ext} = 21.2$ mT—the outer left and

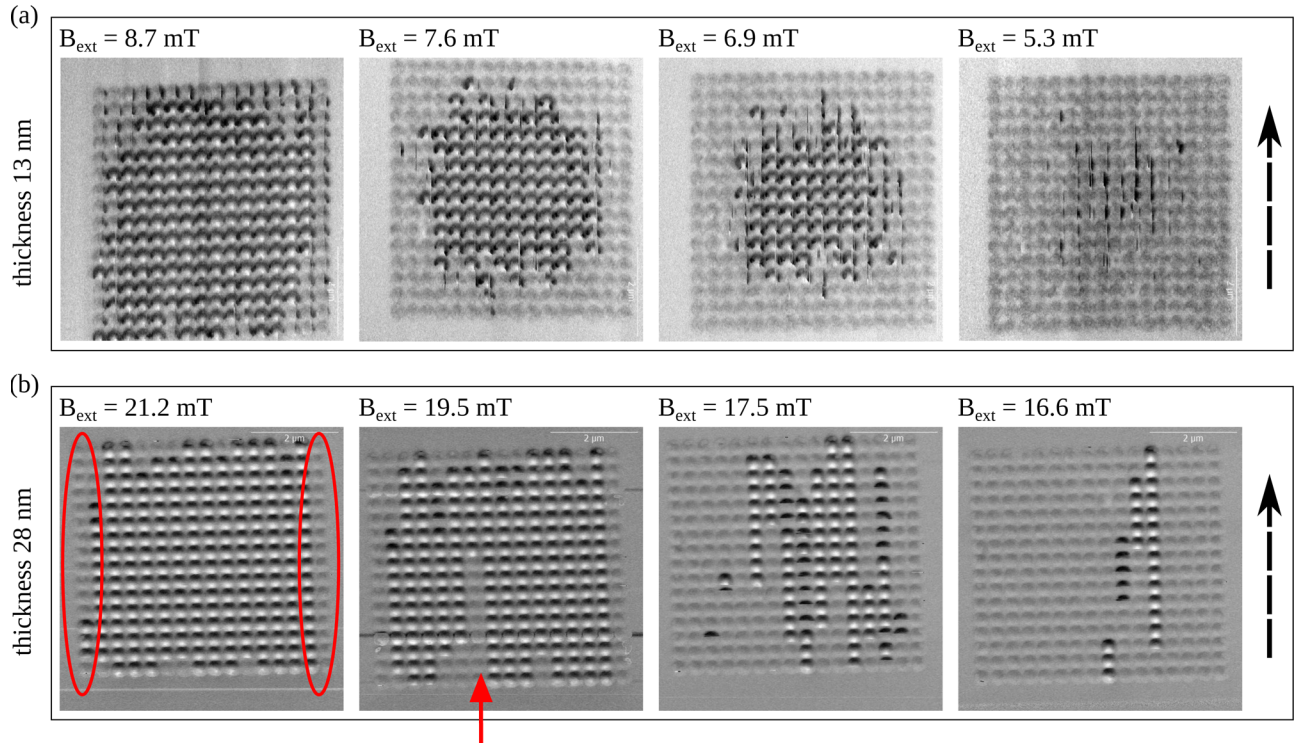

FIG. 5. Magnetic Force Microscopy (MFM) measurements of dot arrays consisting of 16 × 16 dots with periodicity 400 nm, dot diameter 315 nm, and thickness 13 nm—panel (a)—and 28 nm—panel (b). A large, saturating external field is slowly reduced along the direction indicated with the dashed arrows. (a) The circular arrangement of dots in the S-shape ($B_{ext} = 7.6$ mT and $B_{ext} = 6.9$ mT) evidences the dominance of GCA. (b) Due to GCA, the outer left and right columns go first to the vortex state. Later in the reversal process, NNM dominates as reflected by the long vertical magnetization chains appearing from $B_{ext} = 19.5$ mT (indicated with the red arrow). Images in panel (a) are obtained with a scanning direction parallel to the external field, whereas the scanning direction in panel (b) is perpendicular to the applied field.

right columns have much reduced $\langle B_{ms} \rangle$, see Fig. 1(c)—and that NNM interactions dominate the next stages of the array reversal process—note, e.g., the long central vortex chain indicated with the arrow at $B_{ext} = 19.5$ mT. This complies with our simulations of thicker samples.

CONCLUSION

Depending on their thickness, the cylindrical dots in our studies can go through a vortex or a C-state in order to reduce their magnetic charges. When arranged in arrays, this mechanism leads to different global magnetization reversal processes dominated by GCA or NNM depending on the vortex or C-state formation and on the field at which the state transition occurs. For thicknesses above 15 nm, charge removal occurs via vortex formation. When this takes place at high fields (thicker dots), the reversal is dominated by NNM, whilst when the vortex nucleation happens at low fields, the reversal is dominated by GCA. For thinner dots, the vortex nucleation is strongly reduced in favor of C-states at high fields leading to a completely different reversal process that is dominated by NNM and by the reduced symmetry of the C-state. While we only reported on the samples with varying thickness, we could draw similar conclusions for arrays with different dot diameters. The conclusions are supported by in field MFM imaging once the effect of the stray field of the scanning tip is taken into account.

Based on these findings, we can propose the following design rules: if one aims at obtaining uniform magnetization state distributions throughout the array, we advice to consider arrays with a circular global shape to suppress the effect of GCA in combination with large nanomagnets (thick and/or wide dots) to amplify the effect of NNM interactions. On the other hand, our study also hints at the possibility to achieve non-uniform state distributions of interest by controlling the vortex nucleation fields at the array edges and exploiting the NNM interactions. This might, e.g., enable the propagation of spin wave edge-modes in the vicinity of the vortex magnetization chains nucleated at desired locations.

ACKNOWLEDGMENTS

This work was supported by the Flanders Research Foundation (B.V.d.W.), by the Ministero Italiano dell' Università e della Ricerca (MIUR) under the PRIN2010 Project No. 2010ECA8P3 and FIRB2010 No. RBFR10E61T (S.F.), by the Basque Government Project No. PI_2015-1_19 (P.V. and M.P.), and by the Spanish Ministry of Economy and Competitiveness (MINECO) under the Project No. FIS2015-64519-R (P.V. and M.P.) and through the grant BES-2013-063690 (M.P.).

[1]K. Y. Guslienko, V. Novosad, Y. Otani, H. Shima, and K. Fukamichi, Phys. Rev. B **65**, 024414 (2001).
[2]G. Gubbiotti, M. Madami, S. Tacchi, G. Socino, G. Carlotti, and T. Okuno, Surf. Sci. **600**, 4143 (2006).
[3]A. Vogel, A. Drews, T. Kamionka, M. Bolte, and G. Meier, Phys. Rev. Lett. **105**, 037201 (2010).
[4]K.-M. Wu, L. Horng, J.-F. Wang, J.-C. Wu, Y.-H. Wu, and C.-M. Lee, Appl. Phys. Lett. **92**, 262507 (2008).

[5]S. Urazhdin, D. Demidov, H. Ulrichs, T. Kendziorczyk, T. Kuhn, J. Leuthold, G. Wilde, and O. Demokritov, Nat. Nano **9**, 509 (2014).
[6]V. E. Demidov, S. Urazhdin, H. Ulrichs, V. Tiberkevich, A. Slavin, D. Baither, G. Schmitz, and S. O. Demokritov, Nat. Mater. **11**, 1028 (2012).
[7]V. V. Kruglyak, P. S. Keatley, A. Neudert, R. J. Hicken, J. R. Childress, and J. A. Katine, Phys. Rev. Lett. **104**, 027201 (2010).
[8]S. Tacchi, M. Madami, G. Gubbiotti, G. Carlotti, H. Tanigawa, T. Ono, and M. P. Kostylev, Phys. Rev. B **82**, 024401 (2010).
[9]S. Tacchi, F. Montoncello, M. Madami, G. Gubbiotti, G. Carlotti, L. Giovannini, R. Zivieri, F. Nizzoli, S. Jain, A. O. Adeyeye, and N. Singh, Phys. Rev. Lett. **107**, 127204 (2011).
[10]M. Sepioni, M. Madami, S. Tacchi, G. Gubbiotti, G. Carlotti, D. Bisero, A. O. Adeyeye, N. Singh, and S. Goolaup, J. Phys.: Conf. Ser. **200**, 072089 (2010).
[11]K. Y. Guslienko, J. Nanosci. Nanotechnol. **8**, 2745 (2008); available at http://www.ingentaconnect.com/content/asp/jnn/2008/00000008/00000006/art00003?token=00481d17baec41882ebb17e41225f4038382c3a464c485546735023576b64276ab4856f4.
[12]R. Shindou, R. Matsumoto, S. Murakami, and J.-I. Ohe, Phys. Rev. B **87**, 174427 (2013).
[13]I. Lisenkov, V. Tyberkevych, A. Slavin, P. Bondarenko, B. A. Ivanov, E. Bankowski, T. Meitzler, and S. Nikitov, Phys. Rev. B **90**, 104417 (2014).
[14]B. Van de Wiele, S. Fin, A. Sarella, P. Vavassori, and D. Bisero, Appl. Phys. Lett. **105**, 162407 (2014).
[15]M. Stebliy, A. Ognev, A. Samardak, L. Chebotkevich, R. Verba, G. Melkov, V. Tiberkevich, and A. Slavin, J. Magn. Magn. Mater. **384**, 166 (2015).
[16]E. Nikulina, O. Idigoras, P. Vavassori, A. Chuvilin, and A. Berger, Appl. Phys. Lett. **100**, 142401 (2012).
[17]M. Madami, D. Bisero, G. Gubbiotti, S. Tacchi, G. Carlotti, K. Nakano, and T. Ono, IEEE Trans. Magn. **48**, 1269 (2012).
[18]D. Bisero, P. Cremon, M. Madami, M. Sepioni, S. Tacchi, G. Gubbiotti, G. Carlotti, A. Adeyeye, N. Singh, and S. Goolaup, J. Nanopart. Res. **13**, 5691 (2011).
[19]A. Vansteenkiste, J. Leliaert, M. Dvornik, M. Helsen, F. Garcia-Sanchez, and B. Van Waeyenberge, AIP Adv. **4**, 107133 (2014).
[20]M. Natali, I. L. Prejbeanu, A. Lebib, L. D. Buda, K. Ounadjela, and Y. Chen, Phys. Rev. Lett. **88**, 157203 (2002).
[21]W. Scholz, K. Guslienko, V. Novosad, D. Suess, T. Schrefl, R. Chantrell, and J. Fidler, J. Magn. Magn. Mater. **266**, 155 (2003).
[22]S. Landis, B. Rodmacq, and B. Dieny, Phys. Rev. B **62**, 12271 (2000).
[23]X. Zhu, P. Grütter, V. Metlushko, and B. Ilic, Appl. Phys. Lett. **80**, 4789 (2002).
[24]M. Kleiber, F. Kümmerlen, M. Löhndorf, A. Wadas, D. Weiss, and R. Wiesendanger, Phys. Rev. B **58**, 5563 (1998).
[25]J. Lohau, A. Carl, S. Kirsch, and E. F. Wassermann, Appl. Phys. Lett. **78**, 2020 (2001).